

Simultaneous Fe₃O₄ Nanoparticle Formation and Catalyst-Driven Hydrothermal Cellulose Degradation

Alexander Wotton,* Tracey Yeung, Sreenu Jennepalli, Zhi Li Teh, Russell Pickford, Shujuan Huang, Gavin Conibeer, John A. Stride, and Robert John Patterson



Cite This: *ACS Omega* 2021, 6, 10790–10800



Read Online

ACCESS |



Metrics & More

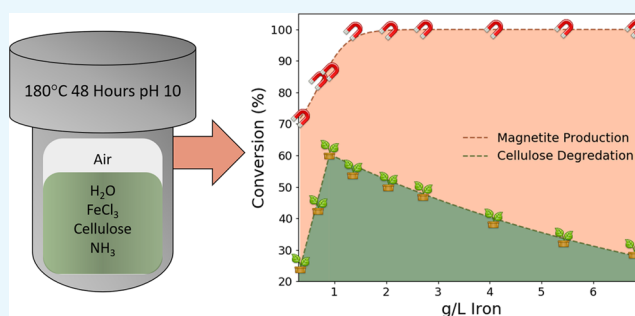


Article Recommendations



Supporting Information

ABSTRACT: Breakdown and utilization of cellulose are critical for the bioenergy sector; however, current cellulose-to-energy conversion schemes often consume large quantities of unrecoverable chemicals, or are expensive, due to the need for enzymes or high temperatures. In this paper, we demonstrate a new method for converting cellulose into soluble compounds using a mixture of Fe²⁺ and Fe³⁺ as catalytic centers for the breakdown, yielding Fe₃O₄ nanoparticles during the hydrothermal process. Iron precursors transformed more than 61% of microcrystalline cellulose into solutes, with the composition of the solute changing with the initial Fe³⁺ concentration. The primary products of the breakdown of cellulose were a range of aldaric acids with different molecular weights. The nanoparticles have concentration-dependent tuneable sizes between 6.7 and 15.8 nm in diameter. The production of value-added nanomaterials at low temperatures improves upon the economics of traditional cellulose-to-energy conversion schemes with the precursor value increasing rather than deteriorating over time.



1. INTRODUCTION

Increasing fossil fuel prices and lower emission targets have driven the development of carbon-neutral biofuels.¹ Biofuels cover a wide gamut of fuel types and uses, including bioethanol, biodiesel, biogas, and syngas.² However, all are derived from the processing and conversion of recently captured carbon from sources such as agricultural crops or marine algae.³ Much work has been done on the optimization of bioenergy feedstocks to maximize energy production.⁴ Researchers have aimed to increase the yield of easily processed carbohydrates and lipids while limiting the relative production of the less energetically valuable, difficult to process cellulosic material.⁵ However, due to the role of cellulose in the structure of plant cell walls, it will always represent a highly significant portion of all plant and algal biomass.⁶ The transformation of cellulose polymers into energetically valuable compounds is thus critical for the bioenergy sector.

Cellulose is the most abundant polymer on earth, representing approximately 70% of all woody matter and up to 33% of the dry weight of microalgae.^{7–9} Chemical and biological cellulose processing methods are the two dominant industrial-scale cellulose-to-energy conversion schemes.¹⁰ During chemical energy extraction, cellulose is often exposed to strong acids and high temperatures, creating glucose monomers after cleaving glycosidic bonds.¹¹ Alternatively, biological cellulose processing involves the hydrolytic extraction of sugars by a combination of enzymes and microbes.¹² However, neither

chemical nor biological cellulose-to-energy conversion schemes have achieved wide-scale adoption, largely due to high energetic and economic costs, limiting net energy production and potential value.

Recently, to reduce energy expenditure and maximize net energy yields, lower-temperature pyrolytic and hydrothermal schemes using catalysts have been demonstrated.^{13–16} These catalytic conversions have demonstrated promise with high conversion rates and additional product selectivity. Unfortunately, many of these catalysts show diminishing returns, with even highly robust silica/carbon nanocomposite catalysts optimized for reusability, showing approximately 10% loss after two reuses.¹⁷ Catalytic pyrolysis is impacted by the composition and size of the catalyst, with smaller nanoparticle catalysts performing better than larger, micron-sized structures.¹⁸

Nanoparticles and ions are typically much more reactive than equivalent larger bulk phase particles.¹⁹ The greater catalytic activity of nanoparticles is due to the high surface area to volume ratios and undercoordinated surface atoms, which impact charge

Received: January 21, 2021

Accepted: March 19, 2021

Published: April 14, 2021



transfer, strain, and quantum size effects.²⁰ Undercoordinated atoms increase molecular adsorption by increasing localized charge across the surface of a particle, which selectively attracts oppositely charged molecular regions.²¹ A range of industries uses the high adsorption and molecular selectivity of these undercoordinated surface regions to control redox reactions.²²

Cellulose degradation approaches often aim to optimize the production of specific cellulose breakdown products by modifying the catalysts, buffers, enzymes, and temperatures utilized.²³ Typical cellulose-energy schemes aim to maximize production of specific energetically valuable compounds like monosaccharides, sugar alcohols, and aldaric acids.^{24,25} Aldaric acids are oxidized sugar molecules with carboxylic acid groups on the first and terminal carbon atoms; they are currently primarily used in the production of bioplastics and bio-nylon.²⁶ The US Department of Energy has labeled aldaric acids as one of the twelve most promising platform molecules.²⁷ Typical aldaric acid production schemes involve the oxidation of monosaccharides, often using enzymes, high-value metal catalysts, or nitric acid.^{28–30}

The use of iron catalysts has been extensively demonstrated to act upon a wide variety of organics.^{31–35} The impact of nanomaterials and iron ions has been examined as catalysts for cellulose and cellulose-based organic degradation, with a variety of different approaches taken. The use of magnetic nanoparticles attached to cellulase demonstrated greatly improved cellulase reusability and a maximum efficiency of 61.94% during the decomposition of corn cobs.³⁶ Magnetic biochar organic anaerobic digestion pretreatments were found to improve methane yields by 11.69%.³⁷ High concentrations of water-soluble iron chloride were found to quickly hydrolyze cellulose, yielding 52% gluconic acid at 110 °C.³⁸ Magnetite nanoparticle-catalyzed thermochemical cellulose decomposition processes demonstrated conversion rates of ~97.5% at 400 °C at pressures approaching 40 MPa. Subsequently, the different approaches, iron species, morphologies, and feedstocks impact the reaction scheme and the products yielded during the degradation. Researchers have even hybridized the cellulose and iron nanoparticles to bio-nanocomposite materials that are capable of acting as highly recyclable catalysts with minimal leaching.^{39,40}

This paper aims to demonstrate an effective novel methodology for the low-temperature conversion of cellulose to smaller, valuable aldaric acids while simultaneously creating value-added nanoparticles. Small quantities of iron nanoparticle precursors greatly assisted the breakdown of cellulose while forming magnetite nanoparticles that may further participate in the breakdown process. The bulk of the catalysis is likely performed by the Fe^{3+} ions, with the catalytic activity decreasing during the formation and growth of the nanoparticles as per ref 38. As such, the catalytic mechanisms and reaction products differ depending on the nucleation rate of iron within the solution (S4). Having magnetite as a product of degradation has some attractive features such as magnetism, nontoxicity, and high industrial demand.^{41,42} The scheme produces energetically valuable aldaric acids, tunable nanoparticle sizes, and high conversion rates of cellulose to soluble derivatives.

2. RESULTS AND DISCUSSION

The process of breaking down cellulose and forming magnetite nanoparticles is complementary. Fe^{3+} acts as a catalyst for the hydrothermal breakdown of cellulose while simultaneously forming Fe_3O_4 nanoparticles of varying sizes. Through the

catalytic action of iron, cellulose is modified into a variety of solutes and to create a nanoparticle coating as well as acting as a reducing agent for Fe^{3+} , allowing for the formation of Fe_3O_4 instead of Fe_2O_3 .

2.1. Particle Characterization. Solids formed post synthesis were characterized to determine features such as size, shape, and compound composition. The crystalline material present within the solid is composed of Fe_3O_4 and crystalline cellulose remnants throughout all initial iron concentrations. The size of the synthesized Fe_3O_4 nanoparticles decreased, with decreasing initial iron concentrations.

All examined samples have consistent crystalline structures, with all XRD peaks maintaining constant locations at various initial iron concentrations (Figure 1). The difference in amplitude between cellulose and Fe_3O_4 peaks increased with

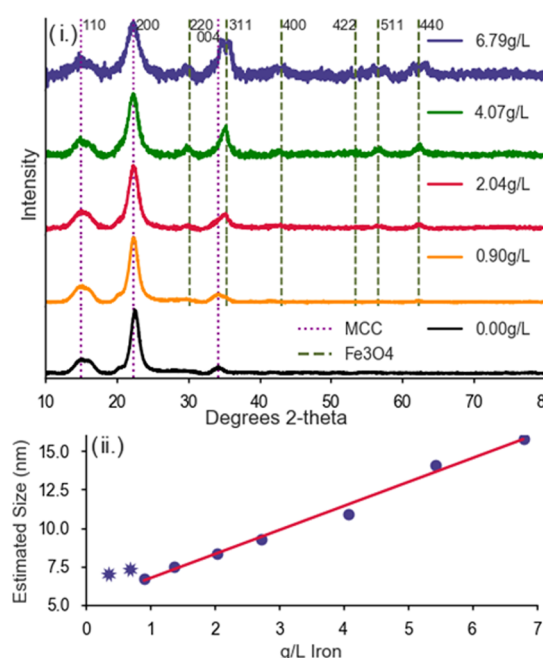


Figure 1. (i) XRD patterns showing cellulosic remnants and Fe_3O_4 nanoparticles at different initial iron concentrations. Cellulose for all samples is at a constant concentration of 66.66 g/L. Iron concentrations are 6.79, 4.07, 2.04, 0.90, and 0.00 g/L. Reflection indices for microcrystalline cellulose (MCC) and Fe_3O_4 are marked in magenta and green, respectively. Peak location and abundance are consistent with the formation of Fe_3O_4 rather than $\gamma\text{-Fe}_2\text{O}_3$, and $\alpha\text{-Fe}_2\text{O}_3$ (Figure S3). Fe_3O_4 peaks have diffraction angles at 29.97, 35.3, 42.90, 53.21, 56.72, and 62.28°, while cellulose has diffraction angles at 15.00, 22.41, and 34.29°. Cellulose diffraction peaks decrease in amplitude and increase in width as the initial iron content increases, suggesting decreased crystallinity and decreased abundance. Magnetite peak widths increase with decreasing initial iron content, suggesting decreased mean particle size or decreased crystallinity. (ii) Estimations of mean particle size via the Scherrer equation. The estimated particle size appears highly dependent on the sample's initial iron concentration, suggesting that one could tune their synthesis to promote desired particle growth. Particle size estimations increased linearly between 0.90 and 6.79 g/L iron. While estimations below a concentration of 0.90 g/L appeared to increase, this is likely due to noise impacting the signal at very low initial iron concentrations rather than a true increase in particle size. The linear fit excluded the points below 0.90 g/L due to the low signal-to-noise ratio. Scherrer equation size estimations are rough as such a variation of up to 20% may be expected, and further size confirmation via TEM is required (Figure 2).

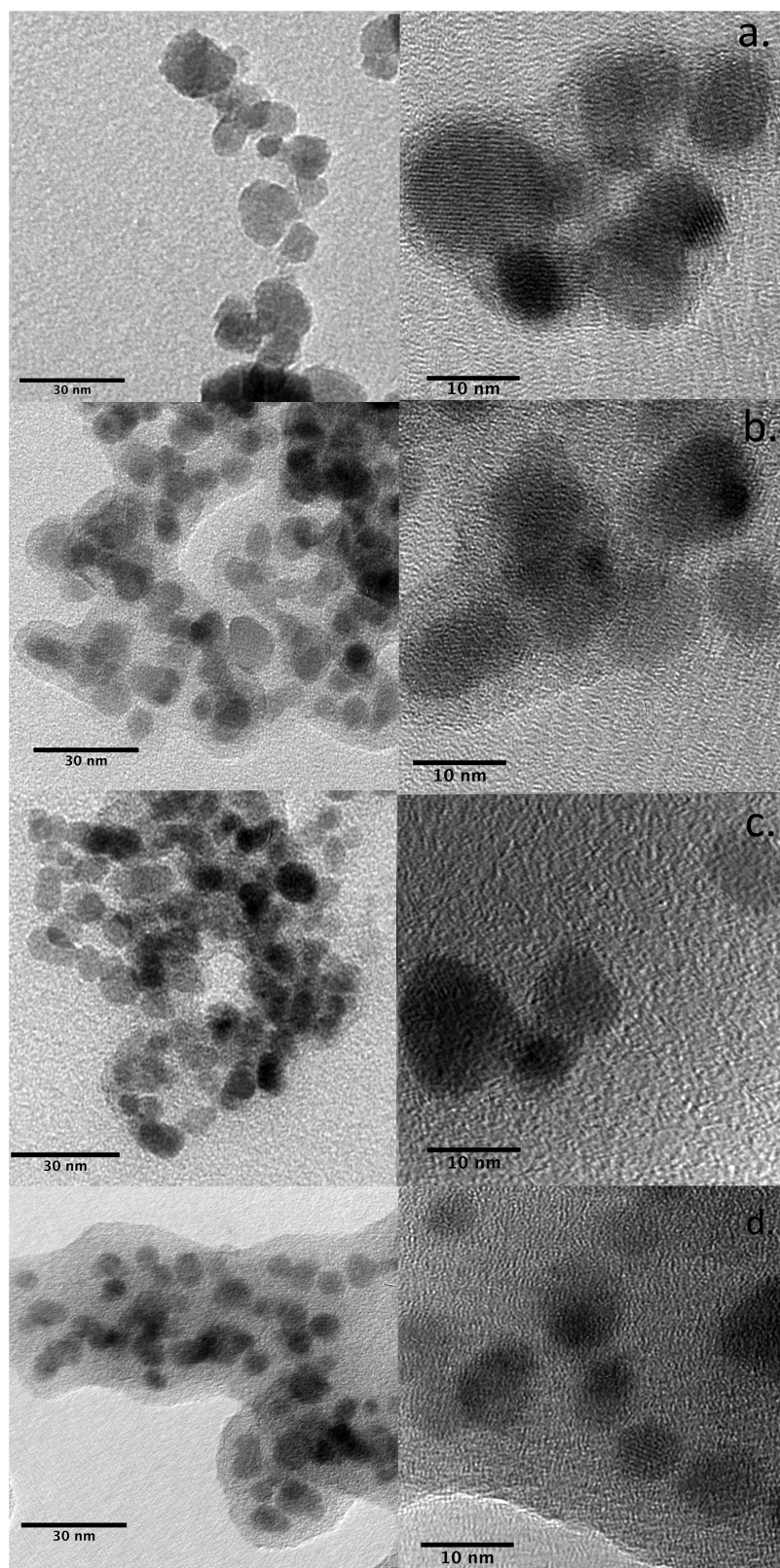


Figure 2. TEM images showing particles synthesized with different initial iron contents at two different magnification levels. Initial iron concentrations are as follows: (a) 6.79 g/L, (b) 4.07 g/L, (c) 2.04 g/L, and (d) 0.90 g/L. Particle size appears to increase with increasing iron content, and measured particle sizes were similar to those estimated by the Scherrer equation. All particles possessed an organic coating of a variable thickness.

decreasing initial iron concentrations. The shifting peak amplitudes suggest that increased initial iron concentrations lead to increased crystalline cellulose breakdown, that increased

initial iron contents lead to increased magnetite production, and that lower initial concentrations of iron lead to smaller production magnetite crystals. Crystalline cellulose peaks

broadened and decreased in amplitude with increasing initial iron content. As all samples had the same initial cellulose concentration, the increasing peak width and decreased amplitudes suggest decreased cellulose crystallinity with increasing initial iron content, indicative of breakdown.

When further examined, peak widths of magnetite signals increased with decreasing iron concentrations, indicating a shift toward smaller particle sizes at lower initial iron concentrations, as per the Scherrer equation (Figure 1ii). Particle size was estimated to increase linearly between 0.90 and 6.79 g/L iron concentration, suggesting that, in these conditions, the ratio of organic material to initial iron content plays a significant role in determining the sizes of the nanoparticles produced. TEM images show decreasing particle size with decreasing initial iron content (Figure 2). Particles ranged in size from approximately 14 nm at 6.79 g/L Fe to under 7 nm at 0.90 g/L, which is consistent with the Scherrer estimation. All particles were found within a coating of a variable thickness, suggesting that the breakdown of cellulosic material forms a protective organic coating, limiting particle growth.

The magnetic activity of the nanoparticles increased with decreasing initial iron concentrations (Figure 3). All nano-

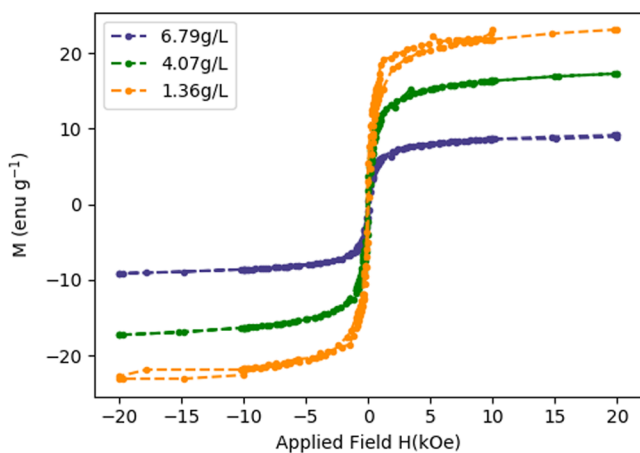


Figure 3. VSM curves showing particles synthesized with initial iron concentrations of 6.79, 4.07, and 1.36 g/L. All samples exhibit minimal hysteresis, coercivity, and remanence, indicating that the nanoparticles are likely all superparamagnetic regardless of the initial iron concentration. The saturation magnetization increases with decreasing initial iron concentrations, likely due to increased organic surface passivation. At 6.79 g/L, saturation occurs at 9.2 emu g⁻¹, while at 4.07 g/L, saturation increases to 17.3 emu g⁻¹. Finally, a maximum saturation magnetization value of 23.1 emu g⁻¹ is achieved by the 1.36 g/L sample.

particle samples exhibited superparamagnetism at room temperature with minimal hysteresis, coercivity and remanence observed in VSM, as expected, given their single domain and small size <15 nm.⁴³ Saturation maxima increased with decreasing iron concentrations from a low maximum of 9.15 emu g⁻¹ at 6.79 g/L iron to a high maximum of 23.1 emu g⁻¹ at 1.36 g/L iron. The results are significantly lower than bulk phase magnetite, which saturates at 92 emu g⁻¹.^{44,45} The lower maxima are typical of coated nanoparticles, with pure magnetite nanoparticles exhibiting maxima between 55 and 75 emu g⁻¹ without organic coatings and decreasing to as low as 3.7 emu g⁻¹ with coatings.^{45–47} Typically, saturation maximums increase with decreasing particle size.⁴⁸ However, in this case, maxima get larger as particles become smaller, likely due to increased particle

surface passivation with increased nanoparticle size.⁴⁹ Higher-iron-content samples nucleate more rapidly than lower-iron-content samples (Figure 9), allowing for greater passivation rates, altering the cellulose conversion to soluble organics, as observed in Figure 11.

During the synthesis of the Fe₃O₄ nanoparticles, cellulose is broken down and modified into a coating agent. Fourier transform infrared (FTIR) spectroscopy results indicate a greater presence of double-bonded oxygen groups within the processed solid organic matter (Figure 4). Each strand of

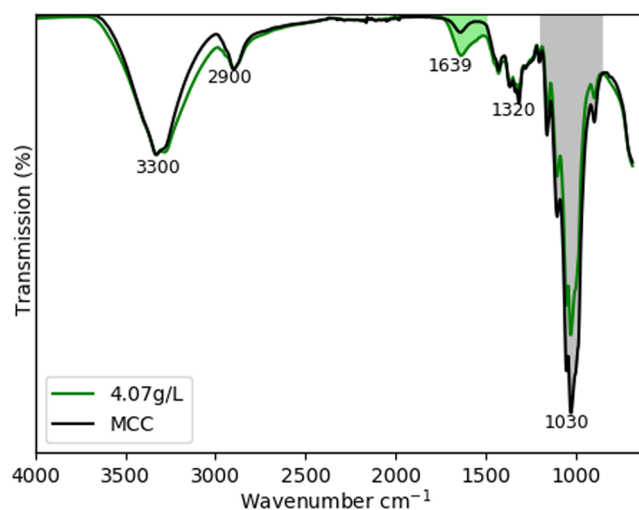


Figure 4. FTIR spectra of unprocessed microcrystalline cellulose and the solid produced by 4.07 g/L Fe synthesis. FTIR spectra of samples were very similar to that of the unprocessed microcrystalline cellulose, suggesting minimal structural changes that occurred to the solid during synthesis. However, in the green shaded area at 1639 cm⁻¹, the double-bonded oxygen stretch increased in relative abundance in the sample post synthesis, suggesting the shortening of cellulose chain lengths. A decrease in the relative transmission in the gray shaded area at 1030 cm⁻¹ corresponding to the C–O–C stretch further suggests that substantial depolymerization occurred during the reaction.

cellulose terminates into two end groups, a nonreducing end and a reducing end, with an aldehyde group. Subsequently, the increased abundance of double-bonded oxygen atoms suggests a shortening of the mean cellulose chain length, increasing the abundance of aldehyde or carboxylic acid end groups. The organics' polar functional groups have likely orientated around the Fe₃O₄ nanoparticles, which could potentially disrupt the hydrogen bonding between cellulose strands, decreasing the tensile strength and resulting in more amorphous content. The shortening and reorientation of cellulose strands are further evidenced in Figure 2, which shows organics situated around the nanoparticles rather than in the linear formation possessed by cellulose bundles.

During this synthesis, the cellulose appears to act as a bifunctional agent by providing a reducing functional group to assist the formation of Fe₃O₄ instead of Fe₂O₃ as well as providing the coating and steric hindrance required to impact the particle size during the breakdown. This process appears possible through the breakdown of cellulose to reducing intermediaries, which is likely assisted by the catalytic activity of Fe³⁺ ions at the beginning of the synthesis.

2.2. Supernatant Characterization. Solutes were characterized to determine the value of the supernatant post hydrothermal treatment. In every examined sample, the pH of

the supernatant produced post synthesis had decreased from the constant presynthesis pH value of 10, indicating the production of acidic molecules or the breakdown of the ammonia across all initial iron concentrations (Figure 5).

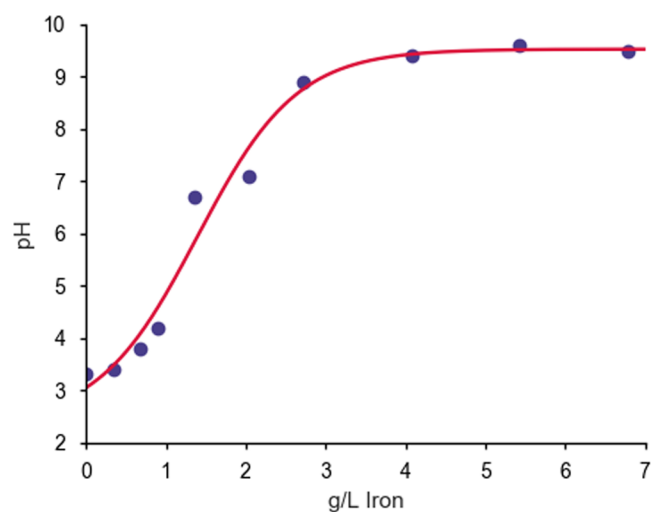


Figure 5. pH measurements post hydrothermal processing. The fit line is a sigmoidal curve. The pH increased exponentially between 0.33 and 2.72 g/L iron before reaching a plateau at 9.5 ± 0.05 at 4.07 g/L, slightly lower than the original presynthesis pH of 10 ± 0.05 . The decrease in pH across all samples is indicative of the production of acids from the cellulose.

The FTIR spectrum of the supernatant possessed consistent peaks across all examined iron concentrations (Figure 6). However, the relative transmission of some peaks changed. In samples produced with higher iron concentrations, the C–H bending at 1457 cm^{-1} possessed a substantially larger peak than the C=O stretching at 1583 cm^{-1} , while samples with lower

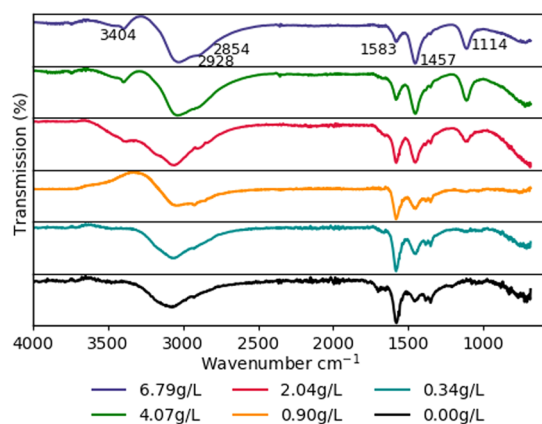


Figure 6. FTIR spectra of supernatants of processed samples after subtracting the background spectrum of water. Iron concentrations are 6.79, 4.07, 2.04, 0.90, 0.68, and 0.00 g/L. Paired peaks at 1583 and 1457 cm^{-1} indicate the presence of conjugated carboxylic acids, further evidenced by an O–H stretch between 3300 and 2500 cm^{-1} . The peak at 1114 cm^{-1} is consistent with the presence of C–O bonds, while peaks at 2928 and 2854 cm^{-1} suggest the presence of C–H₃ and C–H₂ group vibrations, respectively. The peak present at 3404 cm^{-1} likely represents NH₃, and the decrease in transmission with decreasing iron concentrations is due to the lower NH₃ concentrations required to achieve a pH of 10 before synthesis. The FTIR spectra showed no evidence for the production of amines.

initial iron contents had larger peaks corresponding to the C=O stretch than the C–H bend, indicating a change in molecular population at different initial iron contents. The change in peak ratios suggests that the mean carbon chain at higher concentrations of iron is likely to be longer than that at lower concentrations. The C–O stretch at 1114 cm^{-1} decreases in relative amplitude with decreasing iron concentration. The change in peak ratios coincides with the previously mentioned decrease in pH (Figure 5) and is likely due to the carboxylic acid groups' deprotonation at high pH values.

Manual interpretation of the LC–MS measurements allowed observation of compounds at molecular weights of 180, 178, 150, 148, 134, 132, 120, and 118 Da, with the analytes at 180 and 150 possessing the greatest overall abundance/peak area (Figure 7). The data revealed shifts in the observed abundance of solutes

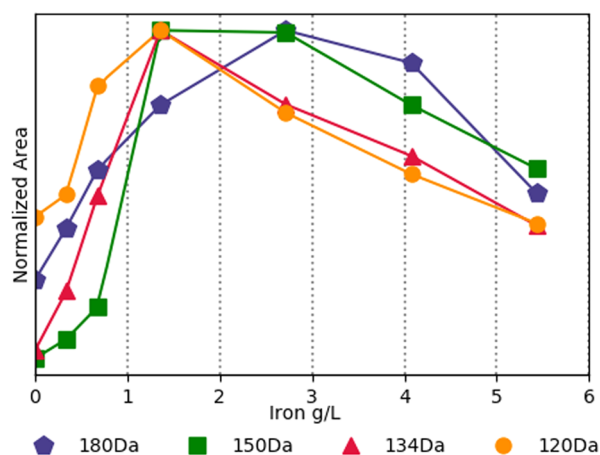


Figure 7. LC–MS results' plotting peak areas obtained from compounds of various molecular weights at differing initial iron concentrations; data points normalized to the highest found area are marked, and a linear interpolation is performed. The molecular weights plotted in this figure are 180, 150, 134, and 120 Da. The observed abundance of compounds is dependent on the compound's molecular weight and the initial iron concentration. Molecules with higher molecular weights were found in greater abundance in samples with higher initial iron contents, while molecules with lower molecular weights had proportionally greater abundance in samples with lower initial iron contents.

depending on the solute's molecular weight and the initial iron concentration. Low-molecular-weight compounds appeared more abundant at lower initial iron concentrations. High-molecular-weight compounds were more abundant at greater initial iron concentrations, confirming our observations from the FTIR analysis (Figure 6). As such, cellulose derivatives appear to undergo further breakdown at lower iron concentrations.

Interestingly, the hydrolysis of cellulose did not produce significant concentrations of monosaccharides. At a molecular weight of 180 Da, retention times of glucose, fructose, galactose, and mannose, run at calibration standards, occurred at between 3.6 and 5.3 min. In contrast, the discovered compound at a molecular weight of 180 Da from the samples had its peak at 1.6 min, suggesting that it is a different compound. The ¹³C glucose internal standard had a retention time of approximately 5.1 min, which corresponded to a separately run glucose standard, indicating that the discovered compounds were likely not monosaccharides. Given the substantially shorter retention time, it is likely that the compounds discovered are more polar than monosaccharides. This conclusion, combined with the

previously mentioned FTIR results, suggests the presence of carboxylic acids at this molecular weight rather than cyclic structures. Similar polar solutes were also likely produced at lower molecular weights with discovered compounds at a molecular weight of 150 Da possessing a retention time of 1.6 min, while external xylose, arabinose, and ribose standards had retention times between 3.1 and 3.9 min.

The production of carboxylic acids likely explains the shift toward lower pH values at lower iron concentrations. It appears likely that the initial product of the cellulose breakdown is a six-carbon sugar, which then undergoes additional reactions, forming shorter chain carboxylic acid groups (Figure 8).

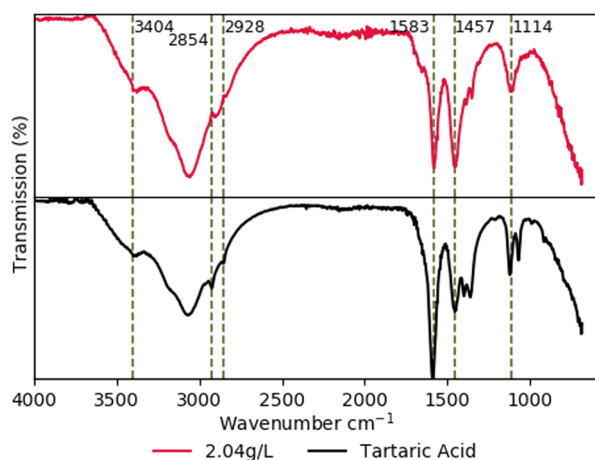


Figure 8. Comparison of FTIR spectra between a sample with an initial iron concentration of 2.04 g/L of iron and tartaric acid prepared in water buffered with ammonia to a pH of 9. Post sampling, both samples had a background spectrum of water subtracted. The green lines show the peak positions common to both samples, suggesting that the compounds produced in the synthesis have a similar structure to tartaric acid.

Subsequently, the increased presence of smaller carboxylic acids creates proportionally more carboxylic acid groups in the supernatant, resulting in the large pH decrease at low initial iron concentrations and explaining the change in the C=O and C–H peak ratios observed in the FTIR spectra.

Results of pH, FTIR, and LC–MS would indicate the presence of molecules with carboxylic acid groups and molecular weights of 180, 150, 134, and 120 Da, suggesting the formation of aldaric acids (Figure 8). The most likely molecular candidates at each discovered molecular weight are pentaric acid at a molecular weight of 180 Da, tartaric acid at a molecular weight of 150 Da, malic acid at 134 Da, and tartronic acid at 120 Da. The Spectral Database for Organic Compounds revealed that these molecules, when paired with a conjugate base, possess similar peaks to those observed.

The low-cost precursors and minimal hazards associated with this synthesis improve upon the safety and economics of typical catalytic aldaric acid production schemes that use high-value metal catalysts and nitric acid.^{29,30} The maximum concentrations for different molecular weights occurred at different iron concentrations, suggesting that there is potential to increase the selectivity of solute production through fine-tuning the initial iron concentration.

2.3. Cellulose Breakdown Efficiency and Soluble Product Yield. Maximum conversions of soluble iron into solid magnetite nanoparticles and maximum conversion of

cellulose into soluble carbohydrates occurred at different initial soluble iron concentrations. Thus, the ideal initial iron concentration is dependent on the desired outcome.

A sigmoidal relationship exists between the conversion percentages of soluble iron into iron nanoparticles across initial iron concentrations between 0.33 and 6.79 g/L (Figure 9).

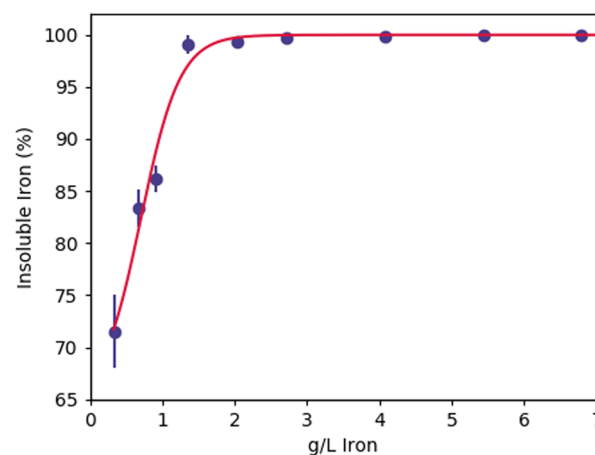


Figure 9. Conversion of soluble iron into an insoluble form. Conversion of soluble iron increased rapidly from 71 to 86% between 0.33 and 0.90 g/L before reaching a plateau at 1.36 g/L, where more than 99% of iron became insoluble.

Soluble iron conversion increased exponentially between 0.33 and 0.9 g/L before reaching a plateau at 1.36 g/L, where more than 99% of iron precursors became solid magnetite nanoparticles. The lower conversion at lower initial iron concentrations is likely due to steric hindrance from the cellulose precursor and cellulose derivative surfactants.⁵⁰ The steric effects of the organics promote slow particle growth, resulting in the desirable smaller nanoparticle sizes. At concentrations less than 0.9 g/L, iron was unable to nucleate completely.

The decreased Fe^{3+} conversion at lower initial iron concentrations likely explains the observed shift toward lower-molecular-weight compounds. Increased Fe^{3+} retention times in samples with low iron contents allow for lengthier catalytic interactions between the soluble iron and cellulose breakdown products. As the particles begin to grow (Figure 1), their catalytic activity becomes increasingly limited as the particles start to take on the properties of the more inert bulk phase. As ICP measurements were taken several weeks after synthesis, leaching is likely not a significant concern at iron concentrations greater than 1 g/L; however, at very low iron concentrations, leaching could be an issue, caused by the greater strain induced during small nanoparticle formation.

Across all initial iron concentrations, TGA analysis revealed the familiar two-stage cellulose volatilization⁵¹ (Figure 10). The initial mass loss at 300 °C represents the hydrolysis of hydroxyl groups, followed by a second hydrolysis stage where residual carbon and Fe_3O_4 undergo oxidation to CO_2 and Fe_2O_3 , respectively. Slight differences within the temperatures and inflection of the two large mass loss events are likely due to different quantities of amorphous organic material and different carbon to oxygen to hydrogen ratios present within the solid. Minor differences in the completion of the two mass loss phases of all samples containing iron occurred between 465 and 485 °C, which was substantially lower than that of pure microcrystalline cellulose, which completed both phases at 542 °C. The lower

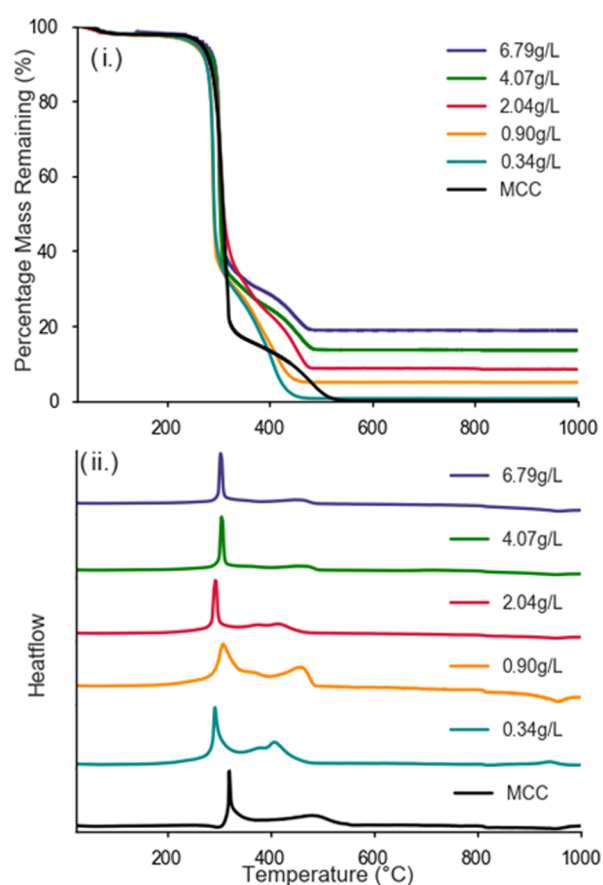


Figure 10. (i) Thermogravimetric analysis (TGA) of samples with different initial iron concentrations between 25 and 1000 °C, heating at 5 °C per minute. Initial iron concentrations are 6.79, 4.07, 2.04, 0.90, and 0.34 g/L Fe, along with unprocessed microcrystalline cellulose. All samples exhibited two-stage organic volatilization with a rapid initial mass loss at approximately 300 °C followed by a secondary mass loss between 325 and 525 °C, leaving a final mass comprised of iron oxides. (ii) Differential scanning calorimetry (DSC) analysis of the same samples present in (i). All samples exhibited two exothermic reactions corresponding with the two stages of mass loss. Widening of the temperature span of reactions at various concentrations of iron indicates a shift toward a more amorphous structure with shorter length carbon chains.

temperature of degradation is likely due to the shortening of the cellulose chains (Figure 4) and creation of a shift toward a more amorphous and less crystalline structure.

DSC analysis of the thermal decomposition showed two exothermic reactions during the mass loss events. The temperature span of the first reaction was variable across all groups examined, ranging from approximately 40 °C at an iron concentration of 6.79 g/L to up to approximately 70 °C at an iron concentration of 0.90 g/L, with the first microcrystalline cellulose-related mass loss event occurring at the smallest temperature range of approximately 30 °C. The increased temperature span of the first reaction is further evidence of a shift toward more amorphous, less uniform shorter chained cellulose structures (Figure 4) as materials with greater crystallinity and uniformity promote more stable, higher-temperature melting points and sharper DSC peaks. Subsequently, it would appear that the sample with 0.90 g/L iron possessed the shortest cellulose chains with chain length increasing sequentially in samples with both higher and lower iron contents. The changing

initial temperature further evidences the shift toward shorter chained amorphous cellulose at the start of the first reaction. The initial temperature of mass loss occurred earliest at 0.90 g/L iron. It exhibited a similar trend to the previously mentioned changes in peak width, with the reaction beginning to occur at increasing temperatures with increasing deviation from the 0.90 g/L sample.

After both large mass loss events, the mass of samples with iron present oscillates slightly as the remaining iron changes oxidation states between Fe_3O_4 , Fe_2O_3 , and FeO . Under 570 °C, Fe_3O_4 and Fe_2O_3 are the only two stable phases of iron, with Fe_2O_3 being the energetically favorable configuration at $-163.7 \text{ kg mol}^{-1}$.⁵² However, above 570 °C, FeO becomes the most stable oxide.⁵³ The oxidation of Fe_3O_4 to Fe_2O_3 likely occurs after the initial cellulosic mass loss, as the protective organic layer is volatilized. This phenomenon can be observed by the apparent appearance of an additional DSC peak between the two cellulosic mass loss events. The oscillations observed in the DSC at higher temperatures are likely due to a phase change between Fe_3O_4 and FeO , which results in a minimal mass loss (Figure 10).

The efficiency of cellulose conversion into soluble compounds across iron concentrations appears to be a two-stage process (Figure 11). The initial stage occurs between 0.33 and

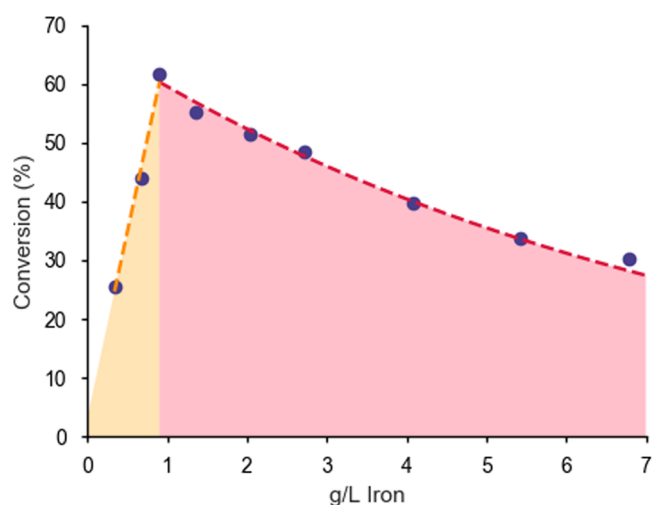


Figure 11. Conversion of cellulose into soluble compounds plotted against the sample concentration of iron. The maximum conversion of cellulose to soluble material of 61.67% occurs at 0.90 g/L iron. At concentrations greater than 0.90 g/L, conversion rates appeared to decrease exponentially with increasing concentrations of iron. At concentrations of iron lower than 0.90 g/L, the conversion efficiency appeared to dramatically decrease to 44.00% at 0.68 g/L and 25.51% at 0.33 g/L iron. Experimental errors for all measurements were less than 0.01%.

0.90 g/L iron, where conversion rates increase sequentially from 25.51 to 61.67%. At these concentrations, the nucleation of nanoparticles was incomplete (Figure 9), suggesting that the sharp linear increase is caused by a limited number of catalytic centers to perform the breakdown. The greatest TON and TOF values were 52.67 mol soluble product/mol Fe catalyst and 26.33 day^{-1} , respectively, achieved at an initial iron concentration of 0.9 g/L. However, given the value-added proposition of the magnetite nanoparticles, catalyst consumption presents itself as an opportunity, rather than a hindrance.

The second stage occurs between 0.90 and 6.79 g/L iron, where conversion rates decrease exponentially from 61.67 to 30.16%. The exponential decay is likely indicative of a two-stage process. Initially, the increased presence of Fe^{3+} allows for a proportionally increased catalytic activity; however, with increased iron concentration, it is likely that the rate of particle nucleation and rate of particle growth is higher. As such, in high-iron-content samples, cellulosic breakdown likely initially occurs very rapidly until particles reach a size where they have a limited capacity to function as catalytic centers. The second stage of breakdown occurs as particles increase in size past that required to be direct catalysts, and the surface area to volume ratio begins to decrease as particles continue to grow. During this growth, the cellulosic coatings orientated around the particles are likely placed under additional strain, creating additional solutes. As initial iron concentrations increase, so do the concentration of chloride ions and the required amount of ammonia to reach a pH of 10. The maximum conversion was achieved at relatively low concentrations of FeCl_3 and NH_3 , indicating that the dominant mechanism of cellulose degradation is the formation of small magnetite nanoparticles rather than the presence of chloride ions or ammonia concentrations. If ammonia or chloride ions were the primary sources of cellulose degradation, conversion efficiency would likely increase with increasing iron/chloride/ammonia content.

The highest conversion efficiencies occurred before the majority of iron became insoluble (Figure 9), suggesting that catalytic activity is either greatly reduced by the formation of nanoparticles or that only the smallest possible particles and ions can act as direct catalysts for the breakdown of cellulose. Based on this insight, it would appear that there is potential to improve efficiency through a further, more detailed examination of concentrations between 0.67 and 1.35 g/L. Furthermore, greater efficiency is likely to be achieved by slowing down the formation of nanoparticles, increasing the length of time during which the iron is acting as a functional catalyst.

3. CONCLUSIONS

Cellulose is the most abundant polymer on earth, and as such, its energetic utilization is essential within the bioenergy space. In this paper, we have introduced and demonstrated an energy scheme that reduces the economic burden of cellulose degradation through the simultaneous production of magnetic nanoparticles. More than 60% of cellulose was converted into soluble compounds, while other cellulosic remnants coated the magnetite particles and minimized particle size. The composition of solutes and the size of nanoparticles are highly tunable. Lower-molecular-weight compounds and smaller particle sizes occur at low initial iron concentrations, whereas heavier compounds and larger nanoparticles form at higher initial iron concentrations. The compounds produced during synthesis predominantly appeared to be aldaric acids that have high utility within the bioenergy and renewables sector. The process improves upon traditional cellulose to energy schemes. It has relevant applications for a variety of industries by providing easily tunable products with precursors that increase in value rather than decrease with time.

4. EXPERIMENTAL METHODS

4.1. Cellulose Degradation Procedure. Various quantities, ranging between 0.08 and 1.64 g of iron chloride hexahydrate ($\text{FeCl}_3 \cdot 6\text{H}_2\text{O}$), were mixed with 3.33 g of

microcrystalline cellulose and stirred in 50 mL of deionized (DI) water. The pH of the solution was increased to 10.0 via the dropwise addition of ammonia (30%). Fifteen milliliters of the sample was then extracted, placed within a Par 25 mL Teflon-lined hydrothermal reactor, and heated in an oven at 180 °C for 48 h. Post processing, 10 mL of DI water was added to assist the removal of all remaining particles from the Teflon liner.

The products were separated to perform characterization of the supernatant and the solids produced during the synthesis. The 25 mL mixture was centrifuged, and the supernatant was poured off and filtered through 33 μm filters to remove any particle agglomerations before being stored in a fridge at 3 °C. Three-quarters of the remaining particles were washed with and stored in ethanol at room temperature, while the remaining quarter was dried in a vacuum oven at 60 °C before particle characterization.

4.2. Particle Characterization. Characterization of the insoluble particle remnants was used to determine the particle size and composition using a combination of transmission electron microscopy (TEM), X-ray powder diffraction (XRD), and Fourier transform infrared (FTIR) spectroscopy.

To determine the particle size, TEM was performed on a Philips CM200. Before TEM imaging, samples were placed in ethanol and ultrasonicated to assist in resuspension and to limit agglomeration, before being drop-cast onto Formvar-coated copper TEM grids. To determine the composition of crystalline forms post synthesis, XRD was performed with an Empyrean I instrument, with scans running between $10^\circ \leq 2\theta \leq 80^\circ$. Crystalline structure identification of organics and iron oxides was performed using the Dataviewer Highscore Plus software package, and the Fe_3O_4 particle size was estimated using the Scherrer equation. FTIR was used to determine the structural changes within the dried solid organic cellulosic remnants. The dried organic cellulosic remnants were scanned on a PerkinElmer spotlight between 4000 and 650 cm^{-1} ; the results were compared to those of the initial microcrystalline cellulose. The products' magnetic properties were examined through vibrating sample magnetometry using a quantum design, physical property measurement system at room temperature with an applied field between +20 and -20 kOe.

4.3. Supernatant Characterization. Functional groups and concentrations of specific compounds present within the supernatant were characterized via a combination of pH testing with a handheld pH meter, FTIR, and liquid chromatography-mass spectroscopy (LC-MS).

A drop of the filtered sample supernatant was placed on a PerkinElmer spotlight 400 FTIR attenuated total reflectance (ATR) crystal, and absorption was measured between 4000 and 650 cm^{-1} . To better display absorption characteristics of the mixed products, DI water was measured, and its spectrum was subtracted from those of the supernatants.

LC-MS was performed on a Q-Exactive HF mass spectrometer with a U3000 chromatography system (Thermo Fisher Scientific); samples were prepared at 20 $\mu\text{g}/\text{mL}$ in 1:1 acetonitrile/water and run for 30 min at 35 °C through a Waters BEH Amide UHPLC column (2.1 \times 100 mm). Mobile phase A was composed of 80:20 MeCN/ H_2O with 0.1% NH_4OH , and mobile phase B was identical except for a 70:30 ratio of MeCN/ H_2O . Commercially available standards for glucose, fructose, galactose, mannose, xylose, ribose, arabinose, deoxyglucose, deoxyribose, and glutaric acid were analyzed as external standards, and a ^{13}C -labeled glucose compound was run across all samples as an internal standard.

4.4. Cellulose Conversion Efficiency. The conversion of soluble iron to nanoparticles and cellulose to soluble carbohydrates was determined using a combination of inductively coupled plasma-mass spectrometry (ICP-MS) and thermogravimetric analysis (TGA).

To determine the elemental conversion efficiency of iron, postsynthesis ICP-MS was utilized. Filtered samples of the supernatants were analyzed, and conversion efficiencies of iron were calculated by dividing the concentration found within the supernatant by the sample's known initial concentration. Total insoluble iron was calculated by subtracting the concentration of iron found in the supernatant from the known initial iron concentration.

A Mettler Toledo TGA/DSC 1 STAR system was used in conjunction with information from ICP, and XRD analysis was used to determine the overall conversion of cellulosic material into soluble carbohydrates. Dry samples were initially weighed on a high-precision 100 μg analytical balance and inserted into the TGA instrument. The TGA instrument was run between 25 and 1000 $^{\circ}\text{C}$ at a heating rate of 5 $^{\circ}\text{C}/\text{min}$, with an airflow rate of 20 mL/min. TGA showed the removal of all cellulosic/insoluble material, consistent with the literature and experimental removal at approximately 400 $^{\circ}\text{C}$, and the final material produced after heating represented a mixed phase of iron oxides comprising mostly Fe_2O_3 as determined by XRD. Mass variation at high temperatures occurred in all iron-containing samples during TGA, which was consistent with the presence of mixed iron oxide phases, including FeO and Fe_2O_3 . To determine the sample's total iron content, the highest mass remaining after 500 $^{\circ}\text{C}$ was assumed to be the mass of pure Fe_2O_3 .



The mass of iron from Fe_2O_3 formed during the TGA was compared to the volatilized cellulose mass to calculate the posthydrothermal treatment ratio of iron to solid organic material. The total insoluble iron ratio to the pretreatment cellulose concentration was then compared to the post-treatment ratio, uncovering the overall conversion of cellulose into soluble derivatives from the hydrothermal treatment.

■ ASSOCIATED CONTENT

SI Supporting Information

The Supporting Information is available free of charge at <https://pubs.acs.org/doi/10.1021/acsomega.1c00393>.

EDS images of the crystalline material obtained post synthesis of a sample containing 5.43 g/L iron (S1), percentage of chlorine found within supernatant (S2), XRD patterns showing cellulosic remnants and Fe_3O_4 nanoparticles at 4.07 g/L initial iron concentration between 25 and 65 $^{\circ}$ (S3), and proposed reaction schematic (S4) (PDF)

■ AUTHOR INFORMATION

Corresponding Author

Alexander Wotton – School of Photovoltaic and Renewable Engineering, University of New South Wales, Kensington, NSW 2052, Australia; orcid.org/0000-0002-1584-9854; Email: a.wotton@unsw.edu.au

Authors

Tracey Yeung – School of Photovoltaic and Renewable Engineering, University of New South Wales, Kensington, NSW 2052, Australia; orcid.org/0000-0001-6402-7585

Sreenu Jennealli – School of Chemistry, University of New South Wales, Kensington, NSW 2052, Australia

Zhi Li Teh – School of Photovoltaic and Renewable Engineering, University of New South Wales, Kensington, NSW 2052, Australia

Russell Pickford – School of Chemistry, University of New South Wales, Kensington, NSW 2052, Australia

Shujuan Huang – School of Photovoltaic and Renewable Engineering, University of New South Wales, Kensington, NSW 2052, Australia; orcid.org/0000-0003-3468-4773

Gavin Conibeer – School of Photovoltaic and Renewable Engineering, University of New South Wales, Kensington, NSW 2052, Australia

John A. Stride – School of Chemistry, University of New South Wales, Kensington, NSW 2052, Australia; orcid.org/0000-0001-9466-8834

Robert John Patterson – School of Photovoltaic and Renewable Engineering, University of New South Wales, Kensington, NSW 2052, Australia

Complete contact information is available at:

<https://pubs.acs.org/10.1021/acsomega.1c00393>

Notes

The authors declare no competing financial interest.

■ ACKNOWLEDGMENTS

A.W. was supported by an Australian Government Research Training Program (RTP) Stipend and the RTP Fee-Offset Scholarship from Federation University Australia.

■ REFERENCES

- (1) Escobar, J. C.; Lora, E. S.; Venturini, O. J.; Yáñez, E. E.; Castillo, E. F.; Almazan, O. *Biofuels: Environment, Technology and Food Security. Renewable Sustainable Energy Rev.* **2009**, *13*, 1275–1287.
- (2) Mohammadi, M.; Najafpour, G. D.; Younesi, H.; Lahijani, P.; Uzir, M. H.; Mohamed, A. R. Bioconversion of Synthesis Gas to Second Generation Biofuels: A Review. *Renewable Sustainable Energy Rev.* **2011**, *15*, 4255–4273.
- (3) Aro, E.-M. From First Generation Biofuels to Advanced Solar Biofuels. *Ambio* **2016**, *45*, 24–31.
- (4) Ferguson, R. M. W.; Villa, R.; Coulon, F. Bioengineering Options and Strategies for the Optimization of Anaerobic Digestion Processes. *Environ. Technol. Rev.* **2014**, *3*, 1–14.
- (5) Liu, J.; Mukherjee, J.; Hawkes, J. J.; Wilkinson, S. J. Optimization of Lipid Production for Algal Biodiesel in Nitrogen Stressed Cells of *Dunaliella Salina* Using FTIR Analysis. *J. Chem. Technol. Biotechnol.* **2013**, *88*, 1807–1814.
- (6) Thomas, L. H.; Forsyth, V. T.; Šturcová, A.; Kennedy, C. J.; May, R. P.; Altaner, C. M.; Apperley, D. C.; Wess, T. J.; Jarvis, M. C. Structure of Cellulose Microfibrils in Primary Cell Walls from Collenchyma. *Plant Physiol.* **2013**, *161*, 465–476.
- (7) Wang, K.; Zhang, J.; Shanks, B. H.; Brown, R. C. The Deleterious Effect of Inorganic Salts on Hydrocarbon Yields from Catalytic Pyrolysis of Lignocellulosic Biomass and Its Mitigation. *Appl. Energy* **2015**, *148*, 115–120.
- (8) Klemm, D.; Heublein, B.; Fink, H.-P.; Bohn, A. Cellulose: Fascinating Biopolymer and Sustainable Raw Material. *Angew. Chem., Int. Ed.* **2005**, *44*, 3358–3393.
- (9) Northcote, D. H.; Goulding, K. J.; Horne, R. W. The Chemical Composition and Structure of the Cell Wall of *Chlorella Pyrenoidosa*. *Biochem. J.* **1958**, *70*, 391–397.

- (10) Jiang, L.; Zheng, A.; Zhao, Z.; He, F.; Li, H.; Wu, N. The Comparison of Obtaining Fermentable Sugars from Cellulose by Enzymatic Hydrolysis and Fast Pyrolysis. *Bioresour. Technol.* **2016**, *200*, 8–13.
- (11) Sasaki, M.; Fang, Z.; Fukushima, Y.; Adschiri, T.; Arai, K. Dissolution and Hydrolysis of Cellulose in Subcritical and Supercritical Water. *Ind. Eng. Chem. Res.* **2000**, *39*, 2883–2890.
- (12) Alvarez, C.; Reyes-Sosa, F. M.; Díez, B. Enzymatic Hydrolysis of Biomass from Wood. *Microbial. Biotechnol.* **2016**, *9*, 149–156.
- (13) Ji, N.; Zhang, T.; Zheng, M.; Wang, A.; Wang, H.; Wang, X.; Chen, J. G. Direct Catalytic Conversion of Cellulose into Ethylene Glycol Using Nickel-Promoted Tungsten Carbide Catalysts. *Angew. Chem.* **2008**, *120*, 8638–8641.
- (14) Tan, X.; Deng, W.; Liu, M.; Zhang, Q.; Wang, Y. Carbon Nanotube-Supported Gold Nanoparticles as Efficient Catalysts for Selective Oxidation of Cellobiose into Gluconic Acid in Aqueous Medium. *Chem. Commun.* **2009**, 7179–7181.
- (15) Lee, H. W.; Kim, Y.-M.; Jae, J.; Jeon, J.-K.; Jung, S.-C.; Kim, S. C.; Park, Y.-K. Production of Aromatic Hydrocarbons via Catalytic Co-Pyrolysis of Torrefied Cellulose and Polypropylene. *Energy Convers. Manage.* **2016**, *129*, 81–88.
- (16) Lazaridis, P. A.; Karakoulia, S. A.; Teodorescu, C.; Apostol, N.; Macovei, D.; Panteli, A.; Delimitis, A.; Coman, S. M.; Parvulescu, V. L.; Triantafyllidis, K. S. High Hexitols Selectivity in Cellulose Hydrolytic Hydrogenation over Platinum (Pt) vs. Ruthenium (Ru) Catalysts Supported on Micro/Mesoporous Carbon. *Appl. Catal., B* **2017**, *214*, 1–14.
- (17) Van de Vyver, S.; Peng, L.; Geboers, J.; Schepers, H.; Clippel, F.; de Gommès, C. J.; Goderis, B.; Jacobs, P. A.; Sels, B. F. Sulfonated Silica/Carbon Nanocomposites as Novel Catalysts for Hydrolysis of Cellulose to Glucose. *Green Chem.* **2010**, *12*, 1560–1563.
- (18) Chaki, S. H.; Mahato, K. S.; Deshpande, M. P. Catalytic Action of CuAlS₂ Microparticles and Nanoparticles in Cellulose Pyrolysis. *Phys. Scr.* **2015**, *90*, No. 045701.
- (19) Khan, I.; Saeed, K.; Khan, I. Nanoparticles: Properties, Applications and Toxicities. *Arabian J. Chem.* **2017**, DOI: 10.1016/j.arabjch.2017.05.011.
- (20) Baraldi, A.; Bianchettin, L.; de Gironcoli, S.; Vesselli, E.; Lizzit, S.; Petaccia, L.; Comelli, G.; Rosei, R. Enhanced Chemical Reactivity of Under-Coordinated Atoms at Pt–Rh Bimetallic Surfaces: A Spectroscopic Characterization. *J. Phys. Chem. C* **2011**, *115*, 3378–3384.
- (21) Tan, Y. C.; Zeng, H. C. Lewis Basicity Generated by Localised Charge Imbalance in Noble Metal Nanoparticle-Embedded Defective Metal–Organic Frameworks. *Nat. Commun.* **2018**, *9*, No. 4326.
- (22) Zhang, S.; Zhang, X.; Jiang, G.; Zhu, H.; Guo, S.; Su, D.; Lu, G.; Sun, S. Tuning Nanoparticle Structure and Surface Strain for Catalysis Optimization. *J. Am. Chem. Soc.* **2014**, *136*, 7734–7739.
- (23) Wang, Y.; Song, H.; Peng, L.; Zhang, Q.; Yao, S. Recent Developments in the Catalytic Conversion of Cellulose. *Biotechnol. Equip.* **2014**, *28*, 981–988.
- (24) Jin, F.; Enomoto, H. Rapid and Highly Selective Conversion of Biomass into Value-Added Products in Hydrothermal Conditions: Chemistry of Acid/Base-Catalysed and Oxidation Reactions. *Energy Environ. Sci.* **2011**, *4*, 382–397.
- (25) Kobayashi, H.; Ito, Y.; Komanoya, T.; Hosaka, Y.; L. Dhepe, P.; Kasai, K.; Hara, K.; Fukuoka, A. Synthesis of Sugar Alcohols by Hydrolytic Hydrogenation of Cellulose over Supported Metal Catalysts. *Green Chem.* **2011**, *13*, 326–333.
- (26) Wu, Y.; Enomoto-Rogers, Y.; Masaki, H.; Iwata, T. Synthesis of Crystalline and Amphiphilic Polymers from D-Glucaric Acid. *ACS Sustainable Chem. Eng.* **2016**, *4*, 3812–3819.
- (27) Werpy, T.; Petersen, G. *Top Value Added Chemicals from Biomass: Volume I—Results of Screening for Potential Candidates from Sugars and Synthesis Gas*. DOE/GO-102004-1992; National Renewable Energy Laboratory: Golden, CO (US), 2004.
- (28) Rautiainen, S.; Lehtinen, P.; Chen, J.; Vehkamäki, M.; Niemelä, K.; Leskelä, M.; Repo, T. Selective Oxidation of Uronic Acids into Aldaric Acids over Gold Catalyst. *RSC Adv.* **2015**, *5*, 19502–19507.
- (29) Venema, F. R.; Peters, J. A.; van Bekkum, H. Platinum-Catalyzed Oxidation of Aldopentoses to Aldaric Acids. *J. Mol. Catal.* **1992**, *77*, 75–85.
- (30) Mehlretter, C. L.; Rist, C. E. Sugar Oxidation, Saccharic and Oxalic Acids by the Nitric Acid Oxidation of Dextrose. *J. Agric. Food Chem.* **1953**, *1*, 779–783.
- (31) Maleki, A.; Ravaghi, P.; Movahed, H. Green Approach for the Synthesis of Carboxycoumarins by Using a Highly Active Magnetically Recyclable Nanobiocomposite via Sustainable Catalysis. *Micro Nano Lett.* **2018**, *13*, 591–594.
- (32) Maleki, A. One-Pot Three-Component Synthesis of Pyrido-[2',1':2,3]Imidazo[4,5-c]Isoquinolines Using Fe₃O₄@SiO₂-OSO₃H as an Efficient Heterogeneous Nanocatalyst. *RSC Adv.* **2014**, *4*, 64169–64173.
- (33) Maleki, A. One-Pot Multicomponent Synthesis of Diazepine Derivatives Using Terminal Alkynes in the Presence of Silica-Supported Superparamagnetic Iron Oxide Nanoparticles. *Tetrahedron Lett.* **2013**, *54*, 2055–2059.
- (34) Maleki, A.; Taheri-Ledari, R.; Rahimi, J.; Soroushnejad, M.; Hajizadeh, Z. Facile Peptide Bond Formation: Effective Interplay between Isothiazolone Rings and Silanol Groups at Silver/Iron Oxide Nanocomposite Surfaces. *ACS Omega* **2019**, *4*, 10629–10639.
- (35) Firouzi-Haji, R.; Maleki, A. L-Proline-Functionalized Fe₃O₄ Nanoparticles as an Efficient Nanomagnetic Organocatalyst for Highly Stereoselective One-Pot Two-Step Tandem Synthesis of Substituted Cyclopropanes. *ChemistrySelect* **2019**, *4*, 853–857.
- (36) Zhang, Q.; Kang, J.; Yang, B.; Zhao, L.; Hou, Z.; Tang, B. Immobilized Cellulase on Fe₃O₄ Nanoparticles as a Magnetically Recoverable Biocatalyst for the Decomposition of Corn cob. *Chin. J. Catal.* **2016**, *37*, 389–397.
- (37) Qin, Y.; Wang, H.; Li, X.; Cheng, J. J.; Wu, W. Improving Methane Yield from Organic Fraction of Municipal Solid Waste (OFMSW) with Magnetic Rice-Straw Biochar. *Bioresour. Technol.* **2017**, *245*, 1058–1066.
- (38) Zhang, H.; Li, N.; Pan, X.; Wu, S.; Xie, J. Direct Transformation of Cellulose to Gluconic Acid in a Concentrated Iron(III) Chloride Solution under Mild Conditions. *ACS Sustainable Chem. Eng.* **2017**, *5*, 4066–4072.
- (39) Maleki, A.; Eskandarpour, V.; Rahimi, J.; Hamidi, N. Cellulose Matrix Embedded Copper Decorated Magnetic Bionanocomposite as a Green Catalyst in the Synthesis of Dihydropyridines and Polyhydroquinolines. *Carbohydr. Polym.* **2019**, *208*, 251–260.
- (40) El-Nahas, A. M.; Salaheldin, T. A.; Zaki, T.; El-Maghrabi, H. H.; Marie, A. M.; Morsy, S. M.; Allam, N. K. Functionalized Cellulose-Magnetite Nanocomposite Catalysts for Efficient Biodiesel Production. *Chem. Eng. J.* **2017**, *322*, 167–180.
- (41) Kolen'ko, Y. V.; Bañobre-López, M.; Rodríguez-Abreu, C.; Carbó-Argibay, E.; Sailsman, A.; Piñeiro-Redondo, Y.; Cerqueira, M. F.; Petrovykh, D. Y.; Kovnir, K.; Lebedev, O. I.; Rivas, J. Large-Scale Synthesis of Colloidal Fe₃O₄ Nanoparticles Exhibiting High Heating Efficiency in Magnetic Hyperthermia. *J. Phys. Chem. C* **2014**, *118*, 8691–8701.
- (42) Yew, Y. P.; Shameli, K.; Miyake, M.; Ahmad Khairudin, N. B. B.; Mohamad, S. E. B.; Naiki, T.; Lee, K. X. Green Biosynthesis of Superparamagnetic Magnetite Fe₃O₄ Nanoparticles and Biomedical Applications in Targeted Anticancer Drug Delivery System: A Review. *Arabian J. Chem.* **2020**, *13*, 2287–2308.
- (43) Li, Q.; Kartikowati, C. W.; Horie, S.; Ogi, T.; Iwaki, T.; Okuyama, K. Correlation between Particle Size/Domain Structure and Magnetic Properties of Highly Crystalline Fe₃O₄ Nanoparticles. *Sci. Rep.* **2017**, *7*, No. 9894.
- (44) Han, D. H.; Wang, J. P.; Luo, H. L. Crystallite Size Effect on Saturation Magnetization of Fine Ferrimagnetic Particles. *J. Magn. Mater.* **1994**, *136*, 176–182.
- (45) Kavousi, F.; Goodarzi, M.; Ghanbari, D.; Hedayati, K. Synthesis and Characterization of a Magnetic Polymer Nanocomposite for the Release of Metoprolol and Aspirin. *J. Mol. Struct.* **2019**, *1183*, 324–330.
- (46) Taghizadeh, S.-M.; Ghoshoon, M. B.; Berenjian, A.; Ghasemi, Y.; Dehshahri, A.; Ebrahiminezhad, A. Impacts of Magnetic Immobiliza-

tion on the Recombinant Proteins Structure Produced in *Pichia Pastoris* System. *Mol. Biotechnol.* **2021**, *63*, 80–89.

(47) Pham, X. N.; Nguyen, T. P.; Pham, T. N.; Tran, T. T. N.; Tran, T. V. T. Synthesis and Characterization of Chitosan-Coated Magnetite Nanoparticles and Their Application in Curcumin Drug Delivery. *Adv. Nat. Sci.: Nanosci. Nanotechnol.* **2016**, *7*, No. 045010.

(48) Mohapatra, J.; Mitra, A.; Bahadur, D.; Aslam, M. Surface Controlled Synthesis of MFe_2O_4 ($M = Mn, Fe, Co, Ni$ and Zn) Nanoparticles and Their Magnetic Characteristics. *CrystEngComm* **2013**, *15*, 524–532.

(49) Sun, X.; Zheng, C.; Zhang, F.; Yang, Y.; Wu, G.; Yu, A.; Guan, N. Size-Controlled Synthesis of Magnetite (Fe_3O_4) Nanoparticles Coated with Glucose and Gluconic Acid from a Single $Fe(III)$ Precursor by a Sucrose Bifunctional Hydrothermal Method. *J. Phys. Chem. C* **2009**, *113*, 16002–16008.

(50) Abu-Much, R.; Meridor, U.; Frydman, A.; Gedanken, A. Formation of a Three-Dimensional Microstructure of Fe_3O_4 -Poly(Vinyl Alcohol) Composite by Evaporating the Hydrosol under a Magnetic Field. *J. Phys. Chem. B* **2006**, *110*, 8194–8203.

(51) John, A.; Ko, H.-U.; Kim, D.-G.; Kim, J. Preparation of Cellulose-ZnO Hybrid Films by a Wet Chemical Method and Their Characterization. *Cellulose* **2011**, *18*, 675–680.

(52) Takeda, M.; Onishi, T.; Nakakubo, S.; Fujimoto, S. Physical Properties of Iron-Oxide Scales on Si-Containing Steels at High Temperature. *Mater. Trans.* **2009**, *50*, 2242–2246.

(53) Bertrand, N.; Desgranges, C.; Poquillon, D.; Lafont, M.-C.; Monceau, D. Iron Oxidation at Low Temperature (260–500 C) in Air and the Effect of Water Vapor. *Oxid. Met.* **2010**, *73*, 139–162.